A Novel Aquatic Propulsor Inspired by Mobuliform Swimming

Cole R. James, Roman G. Sanelli, Pascal D. Spino, Francisco M. F. R. Gonçalves, Conor K. Trygstad,
Néstor O. Pérez-Arancibia, and Konstantin I. Matveev

Abstract—We present a new type of flexible propulsor for *autonomous underwater vehicles* (AUVs), whose design was inspired by biological observation but also includes elements from classical marine hydrodynamics. The interest in bioinspired AUVs with compliant thrusters that can take advantage of fluid-structure interaction phenomena has significantly grown in recent years because many swimming animals still outmatch their human-made counterparts in terms of agility, efficiency, controlled maneuverability, and even in some cases, speed. Most researchers working on bioinspired fluid locomotion believe that systems with flexible thrusters can potentially outperform rigid platforms. The design of the thruster proposed here draws from mobuliform swimming, characterized by the flapping motion of wing-like pectoral fins, but also from traditional hydrodynamic apparatuses that use rigid cambered surfaces to augment thrust production in comparison with flat and symmetric surfaces. Specifically, the fin of the proposed thruster was conceived to oscillate at similar frequencies as those reported for some large batoid fishes (ranging from $0.4\,\mathrm{Hz}$ to $1.0\,\mathrm{Hz}$) and have a large planform area relative to the size of the AUVs to be propelled. Additionally, the fin, with a rectangular area and the very low aspect ratio of 0.7, is allowed to pitch using a passive rotation mechanism, and its flexible membrane is allowed to undulate due to the reactive hydrodynamic forces acting on its structure. By leveraging its ability to undulate and constraining two of its borders, the flexible membrane of the fin is forced to adopt cambered shapes, which are favorable for thrust production, during different phases of a flapping cycle. Experimental results obtained using a grounded setup demonstrate the suitability of the presented approach. Furthermore, a preliminary analysis of the experimental data indicates that, for experimentally-identified optimal flapping conditions, the proposed propulsor is endowed with superior dynamic characteristics in terms of the output-thrust-to-input-power ratio relative to that of a rigid benchmark thruster.

Index Terms—Bioinspired Propulsion, Flapping Fin, Oscillatory Thrust, Fluid-Structure Interaction.

I. INTRODUCTION

Recently, bioinspired aquatic propulsion has received significant attention from researchers working on developing *autonomous underwater vehicles* (AUVs) because the agility, efficiency, and controlled maneuverability exhibited by many swimming animals have not yet been matched by human-made systems propelled by conventional methods [1], [2]. A wide variety of swimming modes exist in nature and have been used as inspiration for designing aquatic propulsors, including oscillation, undulation, pulsation, and sculling (drag-based propulsion) [3]. Here, we propose a flapping-fin flexible thruster that combines an active oscillation with passive pitching and passive undulation

The authors are with the School of Mechanical and Materials Engineering, Washington State University (WSU), Pullman, WA, USA (e-mail: n.perezarancibia@wsu.edu (N. O. Pérez-Arancibia); matveev@wsu.edu (K. I. Matveev)).
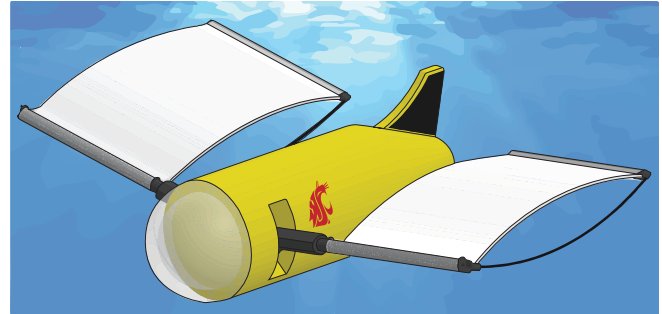
Fig. 1: Conceptual design of an *autonomous underwater vehicle* (AUV) propelled by the proposed stingray-inspired propulsor.

resulting from the interaction of the flexible fin membrane with the surrounding fluid. This design is loosely inspired by the locomotion mechanism employed by large pelagic stingrays (*Pteroplatytrygon violacea*), which is referred to as mobuliform swimming and is characterized by the flapping motion of the wing-like pectoral fins of the animals [4]–[6]. In this type of biological hydrodynamic-thrust production, the oscillating fins are very large relative to the animal body and exhibit moderate to high aspect ratios[1] (ranging from 2.67 to 3.78), thus resembling bird-wing flapping. The inspiration to use mobuliform swimming as a model for developing new propulsors stems from the biological observation that some manta rays can swim in open water for long distances at high speeds, achieving high power and energy efficiency [4].

Ray-inspired propulsors have been developed in the past [5]–[9]. For example, a recent robotic swimmer, the 0.428-meter-long MantaBot, was designed to mimic the oscillation-based locomotion observed in some species of myliobatiformes and thus study mobuliform propulsion [6]. The reported experimental swimming speed is $0.43\,\mathrm{m\cdot s^{-1}}$ at a flapping frequency of $1.1\,\mathrm{Hz}$ and amplitude of about $0.4\,\mathrm{bl}$ (body lengths), which corresponds to a Strouhal number of 0.44, a value very similar to those estimated for mobuliform rays. The design of the MantaBot combines an active biomimetic tensegrity-based structure with a soft body made of silicone, and a cownose ray (*Rhinoptera bonasus*) was scanned using computational tomography to obtain a replicable *three-dimensional* (3D) geometrical model of the animal's shape. In contrast, the thruster proposed in this paper was not designed to mimic mobuliform propulsion but to replicate some of its relevant characteristics, while other features are the result of engineering design based on hydrodynamic considerations. Specifically, we conceived the fin of the propulsor to oscillate at similar frequencies as those reported for large stingrays (ranging from $0.4\,\mathrm{Hz}$

---

[1]Here, we define the aspect ratio of a fin planform as $Æ = s_\mathrm{f}^2 \cdot A_\mathrm{f}^{-1}$, where s_f and A_f are the span and area of the planform, respectively.

to 1.0 Hz) and have a large planform area relative to the size of the propelled vehicle (as depicted in the conceptual design of Fig. 1). However, the fin of the thruster, with the very low aspect ratio of about 0.7 and rectangular shape, pitches passively and its flexible membrane undulates due to the reactive hydrodynamic forces acting on the structure of the system.

The fin-pitching mechanism of the proposed thruster resembles the wing-hinge devices created to passively excite the pitch *degree of freedom* (DOF) of the flapping wings of insect-scale flying robots [10]–[14]. Also, we drew some design elements from the experimental apparatuses described in [15]–[17], used to simultaneously heave and pitch hydrofoils. However, it should be noted that those systems actively excite the pitch DOF of the tested hydrofoils and do not take full advantage of fluid-structure interaction phenomena. The reason for combining design ideas from multiple sources is that our long-term objective is to develop a thruster that simultaneously can reach high propulsive efficiency and leverage fin-water interactions for actuation and control at experimentally-tuned optimal operational conditions. It is important to reemphasize that in the approach introduced here, not only the pitch DOF is excited passively; also, the flexible membrane of the oscillating–pitching fin undulates according to a superposition of several beam vibration modes. This dynamical behavior is relevant and worth further study because it has been reported that passively-excited undulation is common in nature and may play an essential role in aquatic and aerial animal locomotion [18], [19]. In particular, we speculate that alternating positive and negative cambering shapes of a flapping fin during a stroke cycle could have advantages from the power and energy perspectives.

The rest of the paper is organized as follows. Section II presents the design and functionality of the proposed bioinspired propulsor. Section III describes the experimental setup used to characterize the dynamic behavior of the propulsor. Section IV presents and analyzes the main test results. Section V discusses the relevance of the presented research, considering that the obtained experimental data are still preliminary and further work is necessary to reach unquestionable conclusions. Last, Section VI states some conclusions and discusses directions for future research.

Notation:

1) The symbols $\mathbb{R}$ and $\mathbb{Z}$ are used to denote the sets of real and integer numbers, respectively.
2) Regular lowercase letters denote scalars, e.g., a; bold lowercase letters denote vectors, e.g., $\boldsymbol{p}$.
3) The variable $t \in \mathbb{R}$ is used to denote continuous time.
4) The variable $k \in \mathbb{Z}$ is used to index discrete-time signals.
5) The constant $T_s \in \mathbb{R}$ is the sampling period used to discretize continuous-time signals.
6) The symbol t_k denotes discretized time according to $t_k = k \cdot T_s$.
7) The dot operator is used to denote differentiation with respect to time, e.g., $\dot{\alpha}(t) = \frac{d\alpha(t)}{dt}$.

II. DESIGN OF THE PROPULSOR

An illustration of the proposed propulsor and the main variables used to describe its kinematics are shown in Fig. 2(a). Here, we define three frames of reference determined by bases of three orthogonal unit vectors. These

are: (i) an inertial frame, $\mathcal{N} = \{\boldsymbol{n}_1, \boldsymbol{n}_2, \boldsymbol{n}_3\}$, fixed to planet Earth; (ii) a body-fixed frame, $\mathcal{B} = \{\boldsymbol{b}_1, \boldsymbol{b}_2, \boldsymbol{b}_3\}$, with its origin located at the center of mass of the AUV; and (iii) a rotation-mechanism-fixed frame, $\mathcal{P} = \{\boldsymbol{p}_1, \boldsymbol{p}_2, \boldsymbol{p}_3\}$, with its origin located at the center of fin-rotation (flapping + pitching). Note that $\mathcal{P}$ does not rotate jointly with the fin but with the rotation mechanism drawn in dark gray. The entire propulsion system is composed of three fundamental elements: (i) a servomotor that actively flaps the fin of the thruster according to an oscillatory motion; (ii) the already-mentioned rotation mechanism that oscillates about the flapping axis, $\boldsymbol{p}_1$, and enables the passive pitching of the fin, due to fluid-structure interaction, about the pitching axis, $\boldsymbol{p}_2$; and (iii) the fin, which is composed of a flexible membrane and a rectangular elastic frame. According to this configuration, to fully describe the kinematics, and eventually the dynamics, of the fin during operation, we need to describe the movement of $\mathcal{B}$ relative to $\mathcal{N}$; then, the movement of $\mathcal{P}$ relative to $\mathcal{B}$; and, finally, the movement of the fin's leading edge relative to $\mathcal{P}$. This objective can be achieved using homogeneous transformations or quaternions [20]–[22]. However, we omit the specifics because these are unnecessary in the rest of the paper.

In the proposed design, the only actuator of the thruster is the electric waterproof HiTEC D646WP servomotor that flaps the fin. This device can produce a maximum torque of about 1.27 N·m, and its shaft's angular position is *nominally* controllable using internal electromechanical components for feedback. The rotation mechanism is made of *polylactic acid* (PLA) 3D-printed material, has the geometrical dimensions indicated in Fig. 2(b), weighs 28.5 g, and enables the thruster's fin to pitch with a maximum amplitude of 30°. The flexible membrane of the fin is made of *low-density polyethylene* (LDPE) material, weighs 33.5 g, and its geometrical dimensions after installation, as shown in Fig. 2(b), are 99 mm (height) × 152 mm (width) × 1.6 mm (thickness). The elastic rectangular frame, with a total weight of 13.6 g, is composed of two thin metallic elastic beams (upper and lower edges in Fig. 2(b)) and two 3D-printed PLA plastic rods (left and right edges in Fig. 2(b)). Each elastic beam is simply a piece of steel wire with a length of about 155 mm and a diameter of 1 mm; the leading-edge and trailing-edge rods have lengths of 108 mm, and diameters of 10 mm and 8 mm, respectively. The membrane is connected to the frame at two of its edges through rolling cylinders made from 0.1-mm-thick polyethylene film using *cyanoacrylate* (CA) super glue. Thus, we can think of this membrane as a double-connected beam that can pivot at both extremes. Also, its width (152 mm, as shown in Fig. 2(b)) is longer than the internal distance between the two plastic rods to facilitate significant dynamic variations, such as the direction of its camber's convexity, during each flapping cycle. These induced deformations are also facilitated by the elasticity of the side steel beams of the fin's frame, which flex considerably during operation, as seen in the photographic sequence presented in Section IV.

Consistent with the geometrical configuration graphically defined in Figs. 2(a) and (b), we refer to the rod connected to the pitching mechanism as the leading-edge rod and the distal rod as the trailing-edge rod because of the direction of the local incident flow due to the fin's motion (see Figs. 2(c) and (d)). The side metallic beams of the rectangular frame can deform significantly during
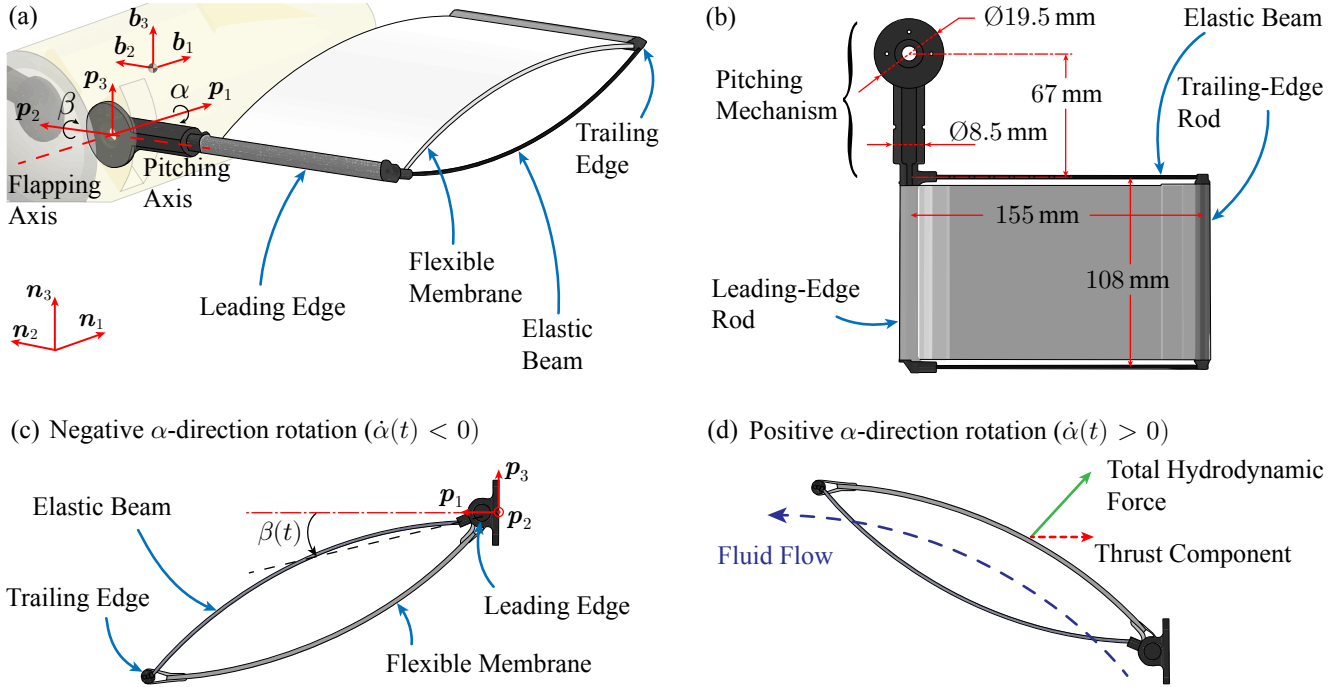
Fig. 2: Illustration of the propulsor, functionality, and frames of reference. **(a)** Main design elements and functional variables of the flapping-fin thruster. We describe the kinematics and functionality of the propulsor using three frames of reference: (i) an inertial frame, $\mathcal{N} = \{n_1, n_2, n_3\}$, fixed to planet Earth; (ii) a body-fixed frame, $\mathcal{B} = \{b_1, b_2, b_3\}$, with its origin located at the center of mass of the AUV; and (iii) a rotation-mechanism-fixed frame, $\mathcal{P} = \{p_1, p_2, p_3\}$, with its origin located at the center of fin-rotation (flapping + pitching). Note that the frame $\mathcal{P}$ does not rotate jointly with the fin but with the rotation mechanism drawn in dark gray. The thruster is composed of three main components: (i) a flapping motor that actively oscillates the fin of the thruster about the flapping axis, p_1; (ii) a rotation mechanism that enables the passive pitching of the fin, due to fluid-structure interaction, about the pitching axis, p_2; and (iii) the fin, which is composed of a flexible membrane and a rectangular elastic frame. The rectangular frame of the fin is composed of two thin elastic beams (side edges), and two plastic rods (leading and trailing edges); the flexible membrane has a thickness of 1.6 mm and is made of *low-density polyethylene* (LDPE) material. The instantaneous flapping angle during operation is $\alpha(t) \in [\alpha_{\min} : \alpha_{\max}]$, for $t \geq 0$, with $0 > \alpha_{\min} \in \mathbb{R}$ and $0 < \alpha_{\max} \in \mathbb{R}$. The instantaneous pitching angle during operation is $\beta(t) \in [\beta_{\min} : \beta_{\max}]$, for $t \geq 0$, with $0 > \beta_{\min} \in \mathbb{R}$ and $0 < \beta_{\max} \in \mathbb{R}$. By definition, for both instantaneous angles, $\alpha(t)$ and $\beta(t)$, signed rotations (positive or negative) about the respective axes, p_1 and p_2, follow the *right-hand convention*; consistently with the definition of the frames $\mathcal{B}$ and $\mathcal{P}$, the neutral position $\{\alpha = 0°, \beta = 0°\}$ occurs when $p_1 = b_1$, $p_2 = b_2$, and $p_3 = b_3$. Note that, regardless of the orientations of $\mathcal{B}$ and $\mathcal{P}$, p_1 is always aligned with b_1. **(b)** Geometrical dimensions of the pitching mechanism and fin that compose the proposed aquatic propulsor. **(c)** Negative α-direction rotation. In this condition, the instantaneous value (0, positive, or negative) of the flapping angle, $\alpha(t)$, decreases and, due to fluid-structure interaction, the instantaneous value (0, positive, or negative) of the pitching angle, $\beta(t)$, increases or reaches saturation. **(d)** Positive α-direction rotation. In this condition, the instantaneous value (0, positive, or negative) of the flapping angle, $\alpha(t)$, increases and, due to fluid-structure interaction, the instantaneous value (0, positive, or negative) of the pitching angle, $\beta(t)$, decreases or reaches saturation.

flapping because they are not attached to the membrane of the fin. The pitching mechanism is simply a shaft that protrudes from the leading-edge rod and passively rotates constrained by the internal surface of a cylindrical tube, as depicted in Fig. 2. As indicated using the rotation-mechanism-fixed reference frame, $\mathcal{P}$, in Fig. 2(a), flapping is defined as the instantaneous rotation, $\alpha(t)$, about the axis p_1 and pitching as the instantaneous rotation, $\beta(t)$, about the axis p_2, for $t \geq 0$. Due to actuation constraints and by design, $\alpha(t) \in [\alpha_{\min} : \alpha_{\max}]$, with $0 > \alpha_{\min} \in \mathbb{R}$ and $0 < \alpha_{\max} \in \mathbb{R}$, and $\beta(t) \in [\beta_{\min} : \beta_{\max}]$, with $0 > \beta_{\min} \in \mathbb{R}$ and $0 < \beta_{\max} \in \mathbb{R}$. Also, by definition, for both $\alpha(t)$ and $\beta(t)$, signed rotations (positive or negative) about their respective axes, p_1 and p_2, satisfy the *right-hand convention*; consistently with the definition of the frames $\mathcal{B}$ and $\mathcal{P}$, the neutral position $\{\alpha = 0°, \beta = 0°\}$ occurs when $p_1 = b_1$, $p_2 = b_2$, and $p_3 = b_3$. Note that, regardless of the orientations of $\mathcal{B}$ and $\mathcal{P}$, p_1 is always aligned with b_1.

As discussed above, flapping is actively generated using a servomotor, while pitching is passively caused by reactive hydrodynamic forces acting on the fin structure and enabled by the rotation mechanism depicted in Fig. 2(b). The resulting pitching motion depends on the friction of

the rotation mechanism and, also, on the geometrical and mechanical properties of both the flexible membrane and the side elastic beams of the fin. A main intended characteristic of this design is that the flexible membrane of the fin is expected to adopt an approximately-convex shape (undulation) during both the upward and downward strokes due to its interaction with the surrounding fluid. However, as explained in Section IV, higher beam-vibration modes are also experimentally observed during operation. Based on biological research that has studied the elastic deformations experienced by insect wings during flapping flight [23]–[25], including dynamic variations of the twist and camber of the aerofoils, we speculate that fins that alternatingly deform to adopt hydrodynamically-favorable convex shapes during the upward and downward strokes could be more effective in deflecting the fluid flow than rigid straight fins. This notion is consistent with research on traditional rigid cambered hydrofoils reported in the marine hydrodynamics literature [26].

By design, the elastic frame of the fin enables the flexible membrane to change its convexity orientation simultaneously with the direction of the pitching-angle variation, as depicted in Figs. 2(c) and (d). As seen here, in agreement with the physics of the situation and the right-hand con-
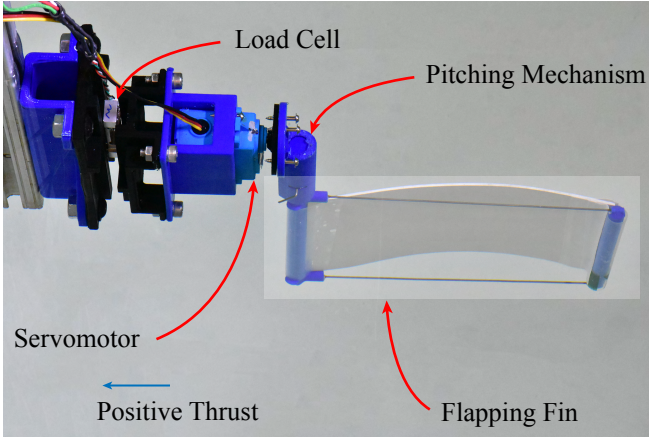
Fig. 3: Photograph of the propulsor prototype used in the experiments discussed in this paper, mounted on the experimental setup. The propulsor is composed of three main components: (i) a servomotor (HiTEC D646WP) that actively flaps the fin of the thruster; (ii) a passive rotation mechanism that enables the pitching motion of the fin due to fluid-structure interaction effects; and (iii) the fin, which is composed of a flexible membrane and an elastic rectangular frame. In this case, to measure the instantaneous thrust produced by the propulsor, we placed a 500-g TAL221 load cell (straight bar, HT Sensor Technology) between the flapping system and its supporting structure. Here, we define thrust as the component of the generated hydrodynamic force that is perpendicular to the stroke plane of the flapping motion.
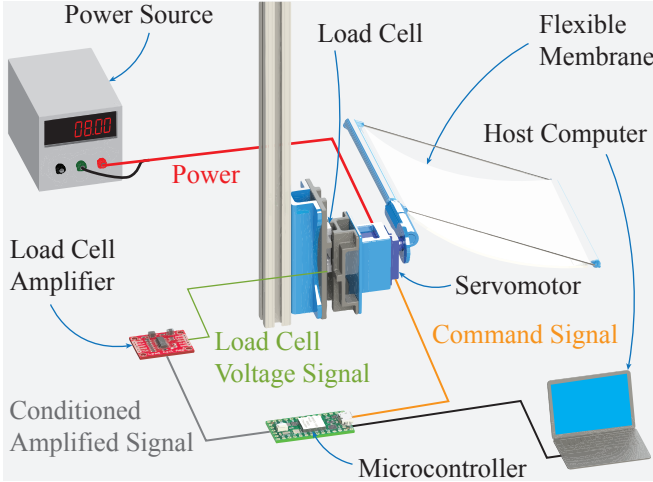

Fig. 4: Illustration of the experimental setup with its main components depicted in a signals-and-systems diagram. Here, the main components are: (i) the tested thruster; (ii) a 500-g TAL221 load cell (straight bar, HT Sensor Technology) used to measure instantaneous thrust; (iii) a signal amplifier (SparkFun HX711) that conditions, amplifies, and digitalizes the raw measurement generated by the load cell; (iv) a microcontroller (ARM Cortex-M7, 600 MHz), mounted on a Teensy 4.0 development board, which generates the command flapping signals that drive the servomotor, and interfaces between a host computer and the load cell amplifier; and (v) a host computer used to interface with the microcontroller board and record the experimental data.

vention, when the flapping rotation is negative ($\dot{\alpha}(t) < 0$), the pitching rotation is positive ($\dot{\beta}(t) > 0$), or saturates ($\dot{\beta}(t) = 0$ and $\beta(t) = \beta_{\max}$), and the membrane deforms as shown in Fig. 2(c); similarly, when the flapping rotation is positive ($\dot{\alpha}(t) > 0$), the pitching rotation is negative ($\dot{\beta}(t) < 0$), or saturates ($\dot{\beta}(t) = 0$ and $\beta(t) = \beta_{\min}$), and the membrane deforms as shown in Fig. 2(d). The rationale behind this design choice is that, as illustrated in Fig. 2(d),

the local (relative to the fin) fluid flow deflected by the vane-shaped surface of the fin's membrane is expected to produce a relatively large hydrodynamic force that is perpendicular to the stroke plane of flapping (thrust).

Specifically, we hypothesize that the proposed thruster should exhibit three main dynamic properties:

(i) Compared to a rigid fin with similar geometrical characteristics, the proposed flexible fin is expected to produce a higher cycle-averaged thrust for the same amplitude and frequency of sinusoidal flapping.

(ii) Compared to a rigid fin with similar geometrical characteristics, the proposed flexible fin is expected to draw less actuation power for the same amplitude and frequency of sinusoidal flapping.

(iii) This third hypothesis connects hypotheses (i) and (ii). Compared to a rigid fin with similar geometrical characteristics, the proposed flexible fin is expected to exhibit a larger ratio of the mean cycle-averaged thrust ($\bar{\bar{f}}_{\text{th}}$ specified in Section IV) to the averaged actuation power ($\bar{p}_{\text{a}}$ specified in Section V).

Through the research presented in this paper, we tested these three hypotheses experimentally, using a custom-made setup that enabled us to measure the instantaneous thrust produced by the proposed flexible fin, and a benchmark rigid fin, during operation. These tests are only preliminary; consequently, the experimental results presented here should not be considered conclusive but just the starting point in a long-term research program.

III. EXPERIMENTAL SETUP

A photograph of the propulsor prototype that we fabricated to perform experimental tests is shown in Fig. 3. This device was constructed with exactly the same characteristics and parameters already specified in Section II and, during the experiments, the fin was operated underwater at the four predefined flapping test frequencies in the set $\{0.4, 0.6, 0.8, 1.0\}$ Hz. For each frequency, we used four different amplitudes. To attenuate the effects of fluid-wall interactions during the tests, we used a large volume of water relative to the size of the thruster; precisely, a footprint with an area of $1.15 \text{ m} \times 0.95 \text{ m}$ and a depth of 0.51 m. In this case, relative to the orientation of the photo in Fig. 3, the direction of positive thrust is toward the left, and a 500-g TAL221 load cell (straight bar, HT Sensor Technology) was placed between the flapping mechanism and its rigid supporting structure to measure the generated instantaneous thrust. This load cell can measure forces in the range $[-500 : 500]$ g and was calibrated employing four different laboratory weights: 0 g, 50 g, 100 g, and 200 g. Using the method in [27] and adopting a conservative approach, we determined an upper bound for the total (systematic + random) uncertainty of measurement to be 0.740 g (9.81 mN), which corresponds to about 0.15% of the sensor range. As explained in Section II, thrust is the component of the hydrodynamic force produced by the propulsor that is perpendicular to the stroke plane, i.e., in the direction of $-\boldsymbol{p}_1$, as defined in Fig. 2.

During the tests, the HiTEC D646WP servomotor and TAL221 (500 g) load cell are operated according to the architecture depicted in Fig. 4. Here, the primary physical devices that compose the experimental setup are shown in a systems-and-signals didactic diagram. As seen, a host computer generates the flapping reference that
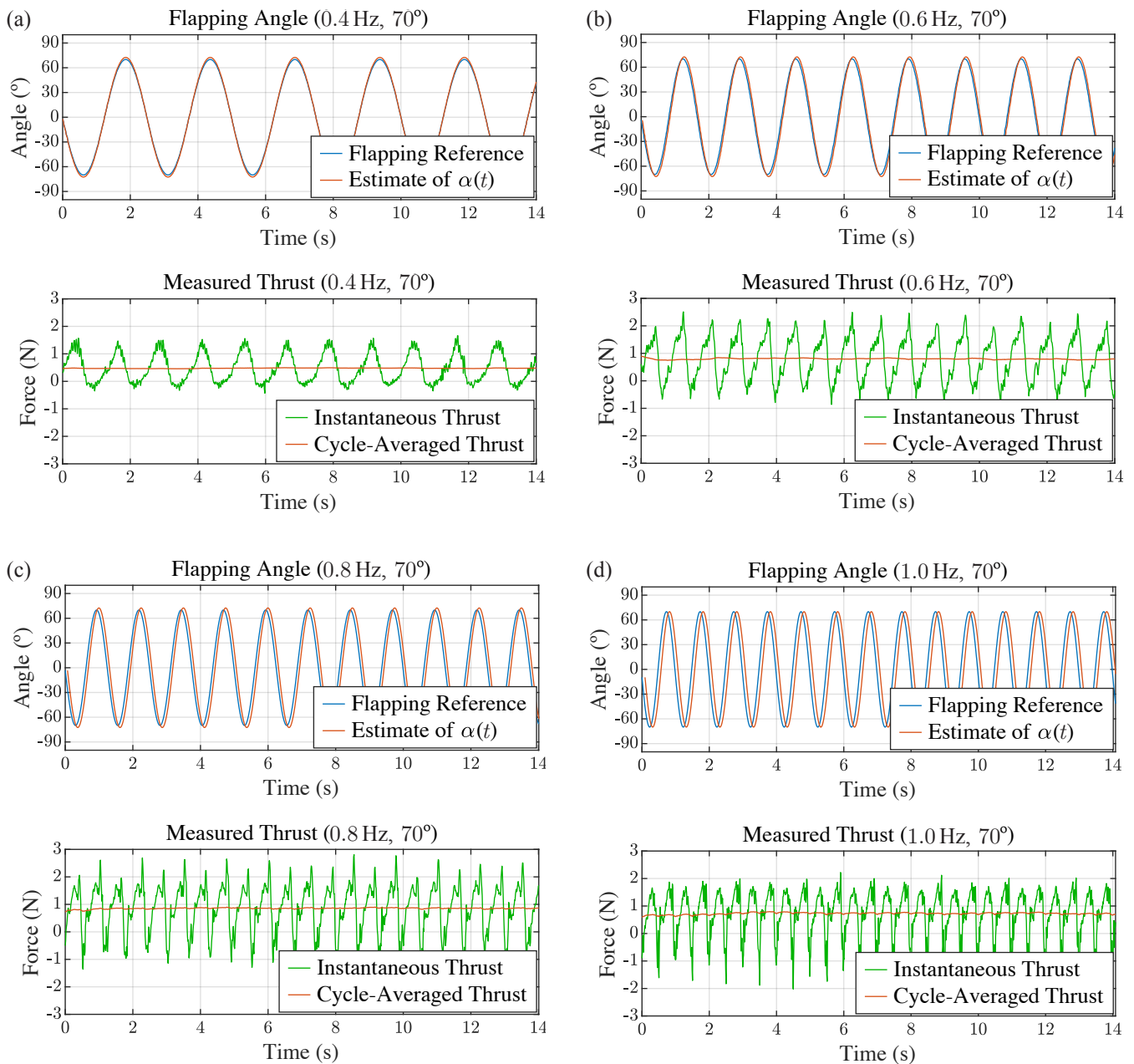
4

Fig. 5: Measured signals obtained through four different flapping-fin experiments in steady state. The four cases presented here correspond to sinusoidal excitations of the servomotor with respective reference frequencies and reference amplitudes of **(a)** $0.4\,\mathrm{Hz}$ and $70°$ ($\alpha_0 \approx 72.5°$ as seen in Table I); **(b)** $0.6\,\mathrm{Hz}$ and $70°$ ($\alpha_0 \approx 72.5°$ as seen in Table I); **(c)** $0.8\,\mathrm{Hz}$ and $70°$ ($\alpha_0 \approx 72.5°$ as seen in Table I); and **(d)** $1.0\,\mathrm{Hz}$ and $70.0°$ ($\alpha_0 \approx 70.0°$ as seen in Table I). Here, the upper plots compare the sinusoidal flapping reference used to excite the thruster's servomotor with an estimate of the resulting instantaneous flapping angle $\alpha(t)$, for $0 \le t \le 14\,\mathrm{s}$. The bottom plots show the measured instantaneous thrust, $f_{\mathrm{th}}(t)$, and the cycle-averaged thrust, $\bar{f}_{\mathrm{th}}(t)$, computed according to (2).

drives the servomotor through an interfacing microcontroller (ARM Cortex-M7 at $600\,\mathrm{MHz}$, mounted on a Teensy 4.0 development board). Note that even though the servomotor uses a feedback mechanism to control the angular position of its shaft, the flapping motion of the thruster is essentially generated in open loop because no external measurement of the instantaneous angle $\alpha(t)$ is used for feedback control. Therefore, as discussed in Section IV, a discrepancy between the servomotor *command signal* indicated in Fig. 4 and the actual signal $\alpha(t)$ is expected. In addition to the command signal, the servomotor receives as an input, through a regular laboratory power source (Kungber SPS3010, $30\,\mathrm{V}$ and $10\,\mathrm{A}$),

the electrical power required to function. In this case, in agreement with the manufacturer's specifications, the voltage is set at $8\,\mathrm{V}$, and the current varies to satisfy the instantaneous requirements of the servomotor. As discussed in Section V, we used this exciting electrical current to estimate the efficiency of the proposed flexible fin relative to that of a benchmark rigid fin.

As expected, given the principles of operation, the raw output voltage generated by the TAL221 ($500\,\mathrm{g}$) load cell used to measure instantaneous thrust is very low and noisy. Therefore, before recording the measured thrust, we filter this signal using a SparkFun HX711 board, which functions

5

TABLE I: ESTIMATED VALUES OF α_0 AND ϕ FOR AN AMPLITUDE REFERENCE OF $70°$, AND MEAN CYCLE-AVERAGED THRUST.

Frequency (Hz)	Estimate of α_0 (°)	Estimate of ϕ (°)	$\bar{\bar{f}}_{\text{th}}$ (N)
0.4	72.5	0.0	0.48
0.6	72.5	7.1	0.78
0.8	72.5	19.3	0.85
1.0	70.0	32.4	0.71

as an analog conditioner, amplifier, and 24-bit analog-digital converter running at a sampling rate of $80\,\text{Hz}$. As depicted in Fig. 4, the same microcontroller used to generate the reference for the instantaneous angle $\alpha(t)$ reads and re-transmits the digitalized thrust measurement to the host computer. The code used to program the microcontroller was written in C++ using the Arduino *integrated development environment* (IDE). Specifically, the real-time command for the oscillating motion of the servomotor (reference for $\alpha(t)$) is generated with a built-in sinusoidal function that allows for user-defined frequency, amplitude, and offset settings. To enable the microcontroller (Teensy 4.0 board) to read the digitalized thrust signal outputted by the load-cell filter–amplifier (SparkFun HX711), we used a specialized code library provided by SparkFun Electronics. The instantaneous digitalized-thrust and flapping-reference signals are transmitted from the microcontroller to the host computer via USB communication; the host reads the information, including the index-time array associated with the experimental data, through a Python-generated executable.

IV. EXPERIMENTAL RESULTS

To test the proposed propulsor empirically, we performed sixteen back-to-back independent experiments corresponding to sinusoidal servomotor-command signals with frequencies in the set $\{0.4, 0.6, 0.8, 1.0\}\,\text{Hz}$ and amplitudes in the set $\{40, 50, 60, 70\}°$. We chose these values after determining their physical feasibility of generation with the experimental setup described in Section III. Additionally, through simple experimental tests, we determined that the flapper (Fig. 3), as a mapping from the servomotor-command signal to the resulting flapping angle $\alpha(t)$, is approximately a linear system; therefore, since it is essentially excited in open loop because no measurement of $\alpha(t)$ is used for feedback correction, the true flapping signal has the form

$$\alpha(t) = \alpha_0 \sin(2\pi\nu t + \phi), \qquad (1)$$

for $t \geq 0$, where ν is both the reference and true frequency of the flapping motion in Hertz; α_0 is the true amplitude of the flapping motion (but not necessarily that of the command signal); and ϕ is a phase introduced by the approximately-linear dynamics of the flapper.

The data corresponding to four different 14-second-long experiments are presented in Figs. 5(a)–(d). Here, the upper plots compare the reference signal used to excite the servomotor with an estimate of the true flapping angle $\alpha(t)$. In this case, we present an estimate of $\alpha(t)$ and not $\alpha(t)$ because the setup is not instrumented with a sensor capable of measuring this variable. The details about the estimation process are presented in the Appendix. As expected, the estimated instantaneous flapping-angle signals are amplified

delayed versions of the respective references. The estimates of α_0 and ϕ corresponding to all the cases in Fig. 5 are shown in Table I. For these four cases, the corresponding measured instantaneous and cycle-averaged thrust forces are shown in the bottom plots of Fig. 5. In this case, we estimate the cycle-averaged thrust, $\bar{f}_{\text{th}}(k)$, for $k \geq 0$, simply using a one-period moving-average filter with the form

$$\bar{f}_{\text{th}}(k) = \frac{1}{N_c} \sum_{i=0}^{N_c-1} f_{\text{th}}(k-i), \qquad (2)$$

where $f_{\text{th}}(k)$ is the sampled measured thrust at discrete time $t_k = k \cdot T_s$; and N_c is the number of samples per flapping period during the steady state. Note that for (2) to make sense algebraically, $k = 0$ must correspond to an instant at which the system has entered the steady state for at least an entire flapping cycle. In the literature on AUVs, the measurement, or estimation, of cycle-averaged thrust is the primary method to evaluate the performance and efficiency of hydrodynamic propulsors.

In the steady state, $\bar{f}_{\text{th}}(k) = \bar{f}_{\text{th}}(t_k = k \cdot T_s)$ is an instantaneous signal approximately constant over a flapping cycle; however, it may vary significantly over time. Therefore, for the purpose of analysis, we further define the mean of the cycle-averaged thrust as

$$\bar{\bar{f}}_{\text{th}} = \frac{1}{N_e} \sum_{i=1}^{N_e} f_{\text{th}}(i), \qquad (3)$$

which is a constant parameter associated with the entire steady-state section of the considered experiment. Consistently, N_e is the total number of points in the steady-state data sequence. The values of $\bar{\bar{f}}_{\text{th}}$ corresponding to the four tests in Fig. 5 are shown in the last column of Table I. As discussed in Section III, the TAL221 ($500\,\text{g}$) sensor has an estimated measurement uncertainty lower than $0.740\,\text{g}$ ($9.81\,\text{mN}$), which can be considered very low for the tests discussed here. For example, this value corresponds to only about $1.26\,\%$ of the mean cycle-averaged thrust for the flapping parameters in the set $\{\nu = 0.6\,\text{Hz}; \alpha_0 \approx 72.5°\}$, as shown in Table I.

As expected, in all the cases presented in Fig. 5, the measured instantaneous thrust oscillates about a positive bias (cycle-averaged thrust) at a frequency that is exactly twice as large as the frequency of the flapping-angle signal. The resulting mean cycle-averaged thrust values for all the cases in Fig. 5, also shown in Table I, suggest that, as predicted by quasi-steady analyses, as the frequency of flapping is increased, the generated cycle-averaged thrust also increases, provided that the amplitude of flapping remains constant. In this study, the conclusion is not entirely definitive because, in the four experiments presented in Fig. 5, α_0 was not kept constant. We will remedy this experimental issue by employing feedback control to flap the propulsor in future experiments. In Fig. 6, to visualize the kinematics of the propulsor during operation, we show a photographic sequence recorded during a time interval of $1.9\,\text{s}$ for a flapping motion with a frequency of $0.6\,\text{Hz}$ and reference amplitude of $70°$ ($\alpha_0 \approx 72.5°$ as seen in Table I) during steady state.

The photographic composite in Fig. 6 includes an entire flapping cycle corresponding to the same test shown in Fig. 5(b), where at time $t = 4.190\,\text{s}$ (first frame), the estimated flapping angle is zero, i.e., $\alpha(t = 4.190\,\text{s}) \approx 0°$. Note
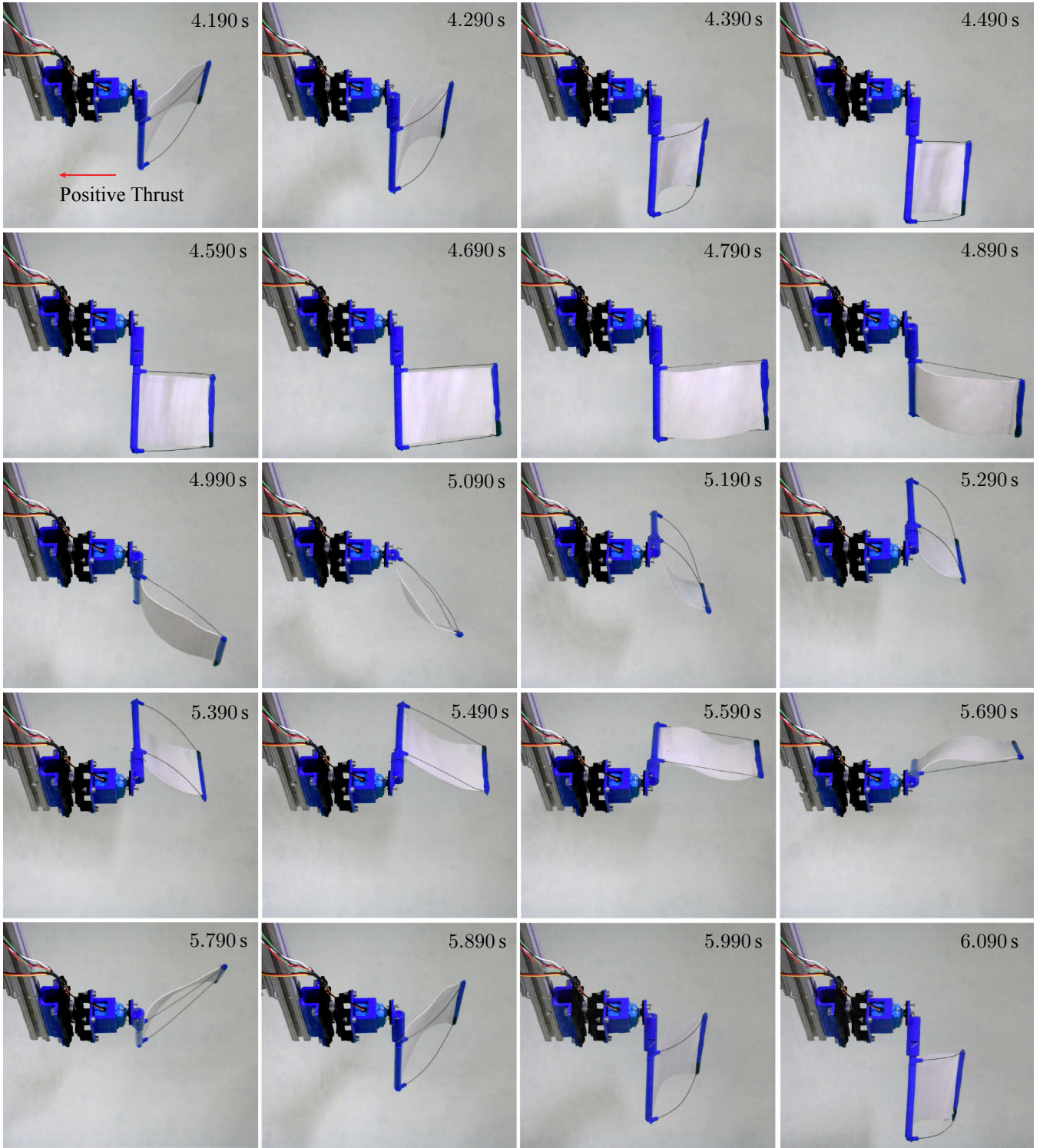
6

Fig. 6: Photographic sequence from video footage of the experiment corresponding to the data in Fig. 5(b), which were obtained using a sinusoidal excitation of the thruster's servomotor with a reference frequency of $0.6\,\mathrm{Hz}$ and reference amplitude of 70° ($\alpha_0 \approx 72.5^\circ$). Here, the frames show twenty different instants during a time interval of $1.9\,\mathrm{s}$, corresponding to a flapping period ($1.\overline{666}\,\mathrm{s}$) plus additional $0.2\overline{33}\,\mathrm{s}$ of data. For the purpose of comparison, note that the first frame in this sequence ($4.190\,\mathrm{s}$) corresponds to the start of a steady-state flapping cycle ($\alpha(t=4.190\,\mathrm{s}) \approx 0^\circ$). As intended by design, during a flapping cycle, the convexity of the fin's membrane switches from negative (relative to the orientation of the photographs in this figure) to positive. Also, as expected, during shape transitions, higher-order vibration modes are clearly observed; for example, see the consecutive frames at times $5.490\,\mathrm{s}$, $5.590\,\mathrm{s}$, and $5.690\,\mathrm{s}$. Last, it is important to note that, as explained in Fig. 2, it can be clearly observed that for a negative α-direction rotation ($\dot{\alpha}(t) < 0$), the β-direction rotation is positive ($\dot{\beta}(t) > 0$); consistently, for a positive α-direction rotation ($\dot{\alpha}(t) > 0$), the β-direction rotation is negative ($\dot{\beta}(t) < 0$).

that, as intended by design and predicted in Section II, these frames show that, in this flapping cycle, for a negative α-direction rotation with respect to $\boldsymbol{p}_1$ ($\dot{\alpha}(t) < 0$), the β-direction rotation is positive with respect to $\boldsymbol{p}_2$ ($\dot{\beta}(t) > 0$); consistently, for a positive α-direction rotation with respect to $\boldsymbol{p}_1$ ($\dot{\alpha}(t) > 0$), the β-direction rotation is negative with
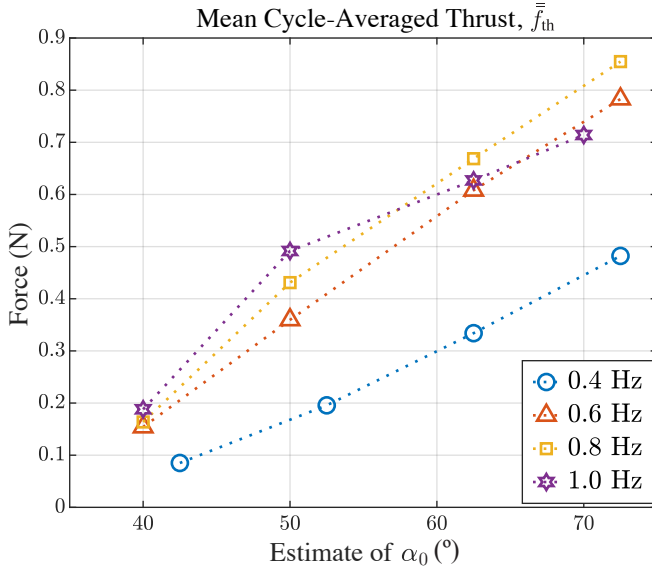
Fig. 7: Mean cycle-averaged thrust, $\bar{\bar{f}}_{\text{th}}$, versus the estimated value of α_0 for sixteen experimental cases. The parameters for the flapping excitation references are the frequencies in the set $\{0.4, 0.6, 0.8, 1.0\}$ Hz and the amplitudes in the set $\{40, 50, 60, 70\}°$. In this case, we used estimates of α_0 and not measured values because the servomotor of the thruster was excited in open loop, and we did not measure the flapping signal $\alpha(t)$ for feedback control.

Fig. 8: Thrust ratio as specified by (4), r_{th}, versus the estimated value of α_0 for sixteen experimental cases. The parameters for the flapping excitation references are the frequencies in the set $\{0.4, 0.6, 0.8, 1.0\}$ Hz and the amplitudes in the set $\{40, 50, 60, 70\}°$. In this case, we used estimates of α_0 and not measured values because the servomotor of the thruster was excited in open loop, and we did not measure the flapping signal $\alpha(t)$ for feedback control.
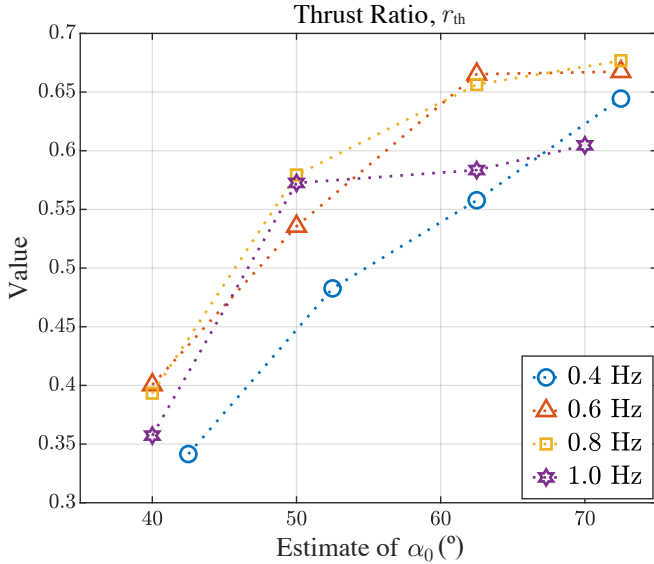
respect to $\boldsymbol{p}_2$ ($\dot{\beta}(t) < 0$). Furthermore, as also predicted in Section II, in this flapping cycle, the shape of the flexible membrane of the thruster alternatingly switched from concave to convex (relative to the orientation of the photos) and, during the shape transition, the membrane exhibits shapes corresponding to high-order modes of vibration.

The mean cycle-averaged thrust forces, computed as specified by (3), for the sixteen experiments discussed here are summarized in Fig. 7. In this case, for the sake of accuracy, we made this plot using an estimate of the flapping amplitude α_0 (identified according to the method described in the Appendix) instead of the reference amplitude sent to the servomotor. This approach makes a direct comparison of all the cases more rigorous but less straightforward. Despite this minor difficulty, we can readily identify some generic patterns. Specifically, it can be immediately seen that the steady-state mean cycle-averaged thrust, $\bar{\bar{f}}_{\text{th}}$, always increases with the estimate of α_0. However, we cannot infer a consistent pattern from these data because for flapping frequencies of 0.4 Hz, 0.6 Hz, and 0.8 Hz, the relationship seems to be linear whereas the relationship for the 1.0-Hz case seems to be nonlinear with a decreasing slope. This decreasing slope for the 1.0-Hz case also suggests that for a fixed large amplitude α_0, in the particular case of the proposed propulsor, increasing the frequency of flapping up to the operational upper bound does not lead to a higher mean cycle-averaged thrust. As also seen in Fig. 7, among the sixteen experimental cases studied in this paper, the two highest mean cycle-averaged thrust values are 0.78 N and 0.85 N, which correspond to the parameter sets $\{\nu = 0.6\,\text{Hz}; \alpha_0 \approx 72.5°\}$ and $\{\nu = 0.8\,\text{Hz}; \alpha_0 \approx 72.5°\}$, respectively (see the estimates for α_0 in Table I). Consistently, regarding potential control strategies based on differential fin flapping for an AUV such as that depicted in Fig. 1, the data indicate that the best frequency of operation is 0.8 Hz because the relationship between the estimate of α_0 and $\bar{\bar{f}}_{\text{th}}$ is both linear and with relatively high force values compared to cases corresponding to the same reference amplitude and frequencies of 0.4 Hz and 0.6 Hz.

A standard secondary metric used to evaluate the performance and efficiency of propulsors is the thrust ratio, defined as

$$r_{\text{th}} = \frac{\bar{\bar{f}}_{\text{th}}}{\bar{f}_{\text{amp}}}, \qquad (4)$$

where $\bar{f}_{\text{amp}}$ is the effective thrust amplitude, here defined as the uncorrected *experimental standard deviation* (ESD) of the measured thrust time-series over the same steady-state interval with N_{e} data points used to compute $\bar{\bar{f}}_{\text{th}}$ as specified by (3); namely,

$$\bar{f}_{\text{amp}} = \sqrt{\frac{2}{N_{\text{e}}} \sum_{i=1}^{N_{\text{e}}} \left[f_{\text{th}}(i) - \bar{\bar{f}}_{\text{th}} \right]^2}. \qquad (5)$$

In general, the thrust ratio r_{th}, as specified by (4), indirectly indicates how effectively an oscillatory force is converted into cycle-averaged thrust. The thrust ratios, r_{th}, for the sixteen experimental cases discussed here, are summarized in Fig. 8. As in the case of Fig. 7, we made Fig. 8 using estimates of the flapping amplitude α_0, not the amplitude reference sent to the servomotor. The resulting plot in Fig. 8 generally exhibits patterns and trends similar to those in Fig. 7. Namely, for flapping frequencies of 0.4 Hz, 0.6 Hz, and 0.8 Hz, the value of the thrust ratio increases with the estimated α_0; however, it is important to note that, in contrast with the curves in Fig. 7, the relationship between r_{th} and the estimate of α_0 for these three frequencies is parabolic and with a decreasing slope as α_0 increases.

The pattern associated with the first three tested flapping frequencies is not continued by that corresponding

8

to $1.0\,\mathrm{Hz}$ as its r_{th} value plateaus and does not change significantly after reaching a value of about 0.57. Similarly to the cases in Fig. 7, among the sixteen tests considered here, the highest values of the r_{th} ratio, 0.67 and 0.68, correspond to the data points $\{\nu = 0.6\,\mathrm{Hz}; \alpha_0 \approx 72.5°\}$ and $\{\nu = 0.8\,\mathrm{Hz}; \alpha_0 \approx 72.5°\}$ in Table I. Therefore, we can confidently conclude that these two operational conditions empirically maximize the generation of mean cycle-averaged thrust (experimental optimal values) and the magnitude of the r_{th} ratio in the considered finite space of parameters. It should be noted, however, that this is an experimental observation, and we do not intend to imply that these conditions and exciting parameters are optimal in the mathematical sense of the word.

After having determined, through multiple tests, that one of the best sets of excitation parameters in the considered finite space is $\{\nu = 0.6\,\mathrm{Hz}; \alpha_0 \approx 72.5°\}$, we further discuss some relevant characteristics of the corresponding instantaneous thrust signal. As seen in the bottom plot of Fig. 5(b), during a force cycle (equivalent to half a flapping cycle), this signal resembles a triangular-shaped periodic function with a two-segment approximately-linear increase and a sudden decrease of the force value. During each thrust period, the measured force reaches local maxima of roughly $2.5\,\mathrm{N}$ at the instants when the estimate of $\alpha(t)$ reaches its local extrema (one maximum and one minimum). Similarly, during each thrust period, the measured force reaches local minima of roughly $-0.5\,\mathrm{N}$, presumably, at the instants when the pitching angle, $\beta(t)$, reverses its direction of change. It is important to reiterate that the measured instantaneous thrust signal oscillates at twice the frequency of flapping because similar thrust patterns are generated in both stroke directions. Note, however, that thrust forces produced during positive and negative α-direction strokes exhibit patterns with slight differences, which can be explained by the existence of minor fabrication errors and assembly misalignments.

Compared to the instantaneous thrust corresponding to the flapping parameter set $\{\nu = 0.6\,\mathrm{Hz}; \alpha_0 \approx 72.5°\}$, for the flapping case corresponding to the parameter set $\{\nu = 0.4\,\mathrm{Hz}; \alpha_0 \approx 72.5°\}$, shown in Fig. 5(a), the local extrema are significantly smaller, and after reaching these values, it takes longer for the instantaneous thrust to cross the signal bias due to slower flapping velocities. This behavior produces smoother sinusoid-like thrust oscillations. Also, as seen in Fig. 5(a), the minima of force do not reach values below $-0.4\,\mathrm{N}$, and the maxima do not surpass $1.7\,\mathrm{N}$. As a result, as shown in Table I, the calculated mean cycle-averaged thrust for this case is only $0.48\,\mathrm{N}$. Additionally, it can be observed that the thrust signal slightly lags the estimated flapping-angle signal and that high-frequency content is quite significant relative to the main component of the measured force. For the flapping case corresponding to the parameter set $\{\nu = 0.8\,\mathrm{Hz}; \alpha_0 \approx 72.5°\}$, shown in Fig. 5(c), the resulting thrust signal generally resembles a higher-frequency version of that corresponding to the $\{\nu = 0.6\,\mathrm{Hz}; \alpha_0 \approx 72.5°\}$ case. For the flapping case corresponding to the parameter set $\{\nu = 1.0\,\mathrm{Hz}; \alpha_0 \approx 70.0°\}$, shown in Fig. 5(d), the measured thrust noticeably lags the flapping motion. Most remarkably, the instantaneous thrust signal looks distorted as its local maxima do not exhibit well-defined peaks and are significantly lower than those corresponding to the $\{\nu = 0.6\,\mathrm{Hz}; \alpha_0 \approx 72.5°\}$ and $\{\nu = 0.8\,\mathrm{Hz}; \alpha_0 \approx 72.5°\}$ cases; additionally, some local minima reach values lower
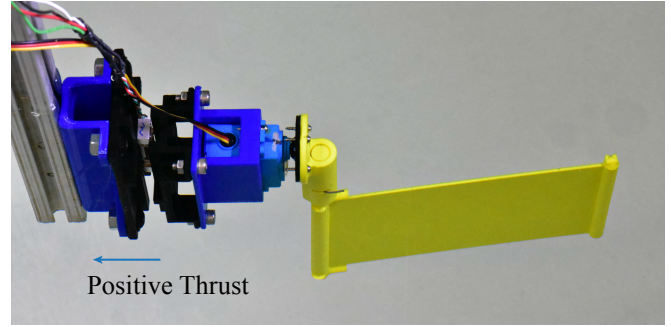

Fig. 9: Photograph of the rigid propulsor used as a preliminary benchmark to compare the performance of the proposed flexible thruster, mounted on the experimental setup presented in Section III. During the discussed experiments, this propulsor was operated under exactly the same conditions as those of the proposed flexible thruster shown in Fig. 3.

than $-1.5\,\mathrm{N}$, which drastically decreases the value of the mean cycle-averaged thrust shown in Table I.

V. DISCUSSION

In this section, we briefly and preliminarily address the hypotheses stated in Section II, using additional experimental data and analyses. For this purpose, we fabricated the 3D-printed PLA rigid thruster shown in Fig. 9, which uses exactly the same mechanisms for flapping and pitching, and roughly has the same geometry as the proposed flexible thruster. Then, we flapped this rigid propulsor with the parameters in the set $\{\nu = 0.6\,\mathrm{Hz}; \alpha_0 \approx 72.5°\}$. For this particular set of flapping parameters, we found the following:

(i) The mean cycle-averaged thrust generated by the rigid thruster is $0.93\,\mathrm{N}$. This value is $19\,\%$ larger than that produced by the flexible thruster with the same flapping parameters. Therefore, these preliminary tests indicate that the first hypothesis stated in Section II is **false**.

(ii) We estimate the average power required for actuation using the voltage, $v_{\mathrm{a}}(t)$, and current, $i_{\mathrm{a}}(t)$, inputted to the servomotor. Specifically, the instantaneous actuation power is computed as $p_{\mathrm{a}}(t) = v_{\mathrm{a}}(t) \cdot i_{\mathrm{a}}(t)$ and the average power, $\bar{p}_{\mathrm{a}}$, as the average of $p_{\mathrm{a}}(t)$ over $14\,\mathrm{s}$ of steady-state data. During operation, we measured both $i_{\mathrm{a}}(t)$ and $v_{\mathrm{a}}(t)$ using a HiLetgo INA219 DC current sensor. For the experiments considered here, the average power consumed by the rigid thruster during the test is $3.94\,\mathrm{W}$, whereas that consumed by the flexible thruster is $2.74\,\mathrm{W}$. Therefore, these preliminary tests indicate that the second hypothesis stated in Section II is **true**.

(iii) Last, to test the third hypothesis stated in Section II, we define as a metric of efficiency the ratio between the mean cycle-averaged thrust, $\bar{\bar{f}}_{\mathrm{th}}$, and the average actuation power, $\bar{p}_{\mathrm{a}}$. Namely,

$$\eta = \frac{\bar{\bar{f}}_{\mathrm{th}}}{\bar{p}_{\mathrm{a}}}. \quad (6)$$

For the experiments considered here, the ratio of efficiency, η, for the rigid thruster is $0.24\,\mathrm{N \cdot W^{-1}}$, whereas for the proposed flexible thruster is $0.28\,\mathrm{N \cdot W^{-1}}$. Therefore, these preliminary tests indicate that the third hypothesis stated in Section II is **true**.

9

VI. CONCLUSIONS

We introduced a new type of bioinspired hydrodynamic flapping propulsor and presented a preliminary experimental study that evaluates its performance. The proposed design includes passive and flexible elements such that multi-DOF motions can be produced with a single actuator by taking advantage of fluid-structure interaction phenomena. To test and demonstrate the suitability of the considered approach, we built both a prototype of the proposed thruster and an instrumented experimental setup. The main components of the experimental setup are a force sensor, used to measure the generated instantaneous thrust, and a camera, used to take video footage of the experiments. Using this measurement system, we performed sixteen different flapping tests and determined that the two best sets of sinusoidal excitation parameters, in order to maximize both mean cycle-averaged thrust and the thrust ratio specified by (4), are $\{\nu = 0.6\,\mathrm{Hz}; \alpha_0 \approx 72.5°\}$ and $\{\nu = 0.8\,\mathrm{Hz}; \alpha_0 \approx 72.5°\}$. Then, using preliminary experimental data, we compared the performance of the proposed flexible thruster with a rigid propulsor used as a benchmark. Inconclusive but promising results indicate that the proposed approach could enable the development of a new generation of bioinspired AUVs.

APPENDIX

Through simple tests, we determined that the flapping system, understood as a mapping from the command signal that excites the servomotor to the resulting flapping angle $\alpha(t)$, is approximately linear. Also, despite using internal feedback mechanisms, the servomotor that drives the studied flexible thruster is essentially operated in open loop because no measurement of the true instantaneous angle $\alpha(t)$ is used for feedback control. As a result, the actual flapping motion is an amplified (or possibly attenuated) and shifted version of the command signal used to excite the servomotor according to the configuration discussed in Section III and depicted in Fig. 4. To find the amplification factor and phase introduced by the flapping mechanism in all the tests discussed in the paper, and correct the experimental data as shown in Fig. 5, we performed a set of simple system-*identification* (system-ID) experiments. We then used video analysis to extract the required correction information.

Specifically, before starting the tests, we placed a digital video camera with its objective lens precisely perpendicular to the motionless $\boldsymbol{p}_2$-$\boldsymbol{p}_3$ plane, as defined in Fig. 2(a). In this arrangement, the objective lens remains aligned with the flapping axis, $\boldsymbol{p}_1$, during operation, and we can capture footage of the instantaneous position of the thruster's leading edge. Then, through offline video processing, we can measure the exact value of the instantaneous angle $\alpha(t)$ at each captured video frame. In each system-ID correction experiment, we used the same servomotor-command signals and replicated exactly the environmental conditions of the thrust-measurement experiments corrected with the estimated gain and phase values. To synchronize a servomotor-command signal with the corresponding captured video frames, an electronic LED-based circuit, controlled with a Teensy 4.0 board, was used to flash a light at each instant the command signal reached an extremum value.

REFERENCES

[1] F. E. Fish, "Advantages of Aquatic Animals as Models for Bio-Inspired Drones Over Present AUV Technology," *Bioinspir. Biomim.*, vol. 15, no. 2, Mar. 2020, Art. no. 025001.

[2] M. I. Lamas and C. G. Rodriguez, "Hydrodynamics of Biomimetic Marine Propulsion and Trends in Computational Simulations," *J. Mar. Sci. Eng.*, vol. 8, no. 7, Jul. 2020, Art. no. 479.

[3] A. J. Smits, "Undulatory and Oscillatory Swimming," *J. Fluid Mech.*, vol. 874, Sep. 2019, P1-1–P1-70.

[4] L. J. Rosenberger, "Pectoral Fin Locomotion in Batoid Fishes: Undulation *Versus* Oscillation," *J. Exp. Biol.*, vol. 15, no. 2, pp. 379–394, Jan. 2001.

[5] F. E. Fish, C. M. Schreiber, K. W. Moored, G. Liu, H. Dong, and H. Bart-Smith, "Hydrodynamic Performance of Aquatic Flapping: Efficiency of Underwater Flight in the Manta," *Aerospace*, vol. 3, no. 3, Sep. 2016, Art. no. 20.

[6] F. E. Fish, H. Dong, J. J. Zhu, and H. Bart-Smith, "Kinematics and Hydrodynamics of Mobuliform Swimming: Oscillatory Winged Propulsion by Large Pelagic Batoids," *Mar. Technol. Soc. J.*, vol. 51, no. 5, pp. 35–47, Sep./Oct. 2017.

[7] K. W. Moored, F. E. Fish, T. H. Kemp, and H. Bart-Smith, "Batoid Fishes: Inspiration for the Next Generation of Underwater Robots," *Mar. Technol. Soc. J.*, vol. 45, no. 4, pp. 99–109, Jul./Aug. 2011.

[8] F. E. Fish, A. J. Smits, H. Haj-Hariri, H. Bart-Smith, and T. Iwasaki, "Biomimetic Swimmer Inspired by the Manta Ray," in *Biomimetics: Nature-Based Innovation*, Y. Bar-Cohen, Ed. Boca Raton, FL, USA: CRC Press, 2012, pp. 495–523.

[9] S. R. Shin, B. Migliori, B. Miccoli, Y.-C. Li, P. Mostafalu, J. Seo, S. Mandla, A. Enrico, S. Antona, R. Sabarish, T. Zheng, L. Pirrami, K. Zhang, Y. S. Zhang, K.-t. Wan, D. Demarchi, M. R. Dokmeci, and A. Khademhosseini, "Electrically Driven Microengineered Bioinspired Soft Robots," *Adv. Mater.*, vol. 30, no. 10, Mar. 2018, Art. no. 1704189.

[10] K. Y. Ma, P. Chirarattananon, S. B. Fuller, and R. J. Wood, "Controlled Flight of a Biologically Inspired, Insect-Scale Robot," *Science*, vol. 340, no. 6132, pp. 603–607, May 2013.

[11] N. O. Pérez-Arancibia, P.-E. J. Duhamel, K. Y. Ma, and R. J. Wood, "Model-Free Control of a Flapping-Wing Flying Microrobot," in *Proc. 16th Int. Conf. Adv. Robot. (ICAR)*, Montevideo, Uruguay, Nov. 2013, pp. 1–8.

[12] ——, "Model-Free Control of a Hovering Flapping-Wing Microrobot," *J. Intell. Robot. Syst.*, vol. 77, no. 1, pp. 95–111, Jan. 2015.

[13] X. Yang, Y. Chen, L. Chang, A. A. Calderón, and N. O. Pérez-Arancibia, "Bee+: A 95-mg Four-Winged Insect-Scale Flying Robot Driven by Twinned Unimorph Actuators," *IEEE Robot. Autom. Lett.*, vol. 4, no. 4, pp. 4270–4277, Oct. 2019.

[14] R. M. Bena, X.-T. Nguyen, X. Yang, A. A. Calderon, Y. Chen, and N. O. Pérez-Arancibia, "A Multiplatform Position Control Scheme for Flying Robotic Insects," *J. Intell. Robot. Syst.*, vol. 105, no. 1, May 2022, Art. no. 19.

[15] M. S. Triantafyllou, G. S. Triantafyllou, and R. Gopalkrishnan, "Wake Mechanics for Thrust Generation in Oscillating Foils ," *Phys. Fluids A: Fluid Dyn.*, vol. 3, no. 12, pp. 2835–2837, Dec. 1991.

[16] G. S. Triantafyllou, M. S. Triantafyllou, and M. A. Grosenbaugh, "Optimal Thrust Development in Oscillating Foils with Application to Fish Propulsion," *J. Fluids Struc.*, vol. 7, no. 2, pp. 205–224, Feb. 1993.

[17] J. M. Anderson, K. Streitlien, D. S. Barrett, and M. S. Triantafyllou, "Oscillating Foils of High Propulsive Efficiency," *J. Fluid Mech.*, vol. 360, pp. 41–72, Apr. 1998.

[18] S. Ramananarivo, R. Godoy-Diana, and B. Thiria, "Rather Than Resonance, Flapping Wing Flyers May Play on Aerodynamics to Improve Performance," *Proc. Natl. Acad. Sci.*, vol. 108, no. 15, pp. 5964–5969, Apr. 2011.

[19] A. Goza, D. Floryan, and C. Rowley, "Connections Between Resonance and Nonlinearity in Swimming Performance of a Flexible Heaving Plate," *J. Fluid Mech.*, vol. 888, Apr. 2020, Art. no. A30.

[20] M. W. Spong, S. Hutchinson, and M. Vidyasagar, *Robot Modeling and Control*. Hoboken, NJ, USA: John Wiley & Sons, 2020.

[21] F. L. Markley and J. L. Crassidis, *Fundamentals of Spacecraft Attitude Determination and Control*. New York, NY, USA: Springer, 2014.

[22] J. B. Kuipers, *Quaternions and Rotation Sequences: A Primer with Applications to Orbits, Aerospace and Virtual Reality*. Princeton, NJ, USA: Princeton University Press, 2002.

[23] A. R. Ennos, "The Inertial Cause of Wing Rotation in Diptera," *J. Exp. Biol.*, vol. 140, no. 1, pp. 161–169, Nov. 1988.

[24] ——, "Inertial and Aerodynamic Torques on the Wings of Diptera in Flight," *J. Exp. Biol.*, vol. 142, no. 1, pp. 87–95, Mar. 1989.

[25] Y. Meresman and G. Ribak, "Allometry of Wing Twist and Camber in a Flower Chafer During Free Flight: How Do Wing Deformations Scale With Body Size?" *R. Soc. Open Sci.*, vol. 4, no. 10, Oct. 2017, Art. no. 171152.

[26] J. N. Newman, *Marine Hydrodynamics*. Cambridge, MA, USA: The MIT Press, 2017.

[27] A. J. Wheeler and A. R. Ganji, *Introduction to Engineering Experimentation*. Upper Saddle River, NJ, USA: Pearson, 2010.